communications physics

ARTICLE

https://doi.org/10.1038/s42005-023-01267-0 OPEN

Optical conductivity and orbital magnetization of Floquet vortex states

Iman Ahmadabadi [1,2]✉, Hossein Dehghani [1,2] & Mohammad Hafezi [1,2]

Motivated by recent experimental demonstrations of Floquet topological insulators, there have been several theoretical proposals for using structured light, either spatial or spectral, to create other properties such as flat bands and vortex states. In particular, the generation of vortex states in a massive Dirac fermion insulator irradiated by light carrying nonzero orbital angular momentum (OAM) has been proposed. Here, we evaluate the orbital magnetization and optical conductivity as physical observables for such a system. We show that the OAM of light induces nonzero orbital magnetization and current density. The orbital magnetization density increases linearly as a function of the OAM degree. In certain regimes, we find that orbital magnetization density is independent of the system size, width, and Rabi frequency of light. It is shown that the orbital magnetization arising from our Floquet theory is large and can be probed by magnetometry measurements. Furthermore, we study the optical conductivity for various types of electron transitions between different states such as vortex, edge, and bulk that are present in the system. Based on the peaks in conductance, a scheme for the detection of vortex states is proposed.

[1] Joint Quantum Institute, University of Maryland, College Park, MD 20742, USA. [2] Quantum Technology Center, University of Maryland, College Park, MD 20742, USA. ✉email: imanah@umd.edu

A class of condensed matter systems which have gained much attraction in recent years are periodically driven materials, known as Floquet systems, that have resulted in a new paradigm for realizing exotic quantum phases of matter[1–12], and some of them have been experimentally realized via optical tools in the last few years[13–15]. Furthermore, there have been recent experimental developments in the spatial manipulation of optical beams for controlling ultra-atomic systems[16–21]. Potentially, applying similar techniques to electronic systems can yield new possibilities for engineering novel quantum phases of matter. In particular, in a recent work[22], it was shown that linearly polarized (LP) or circularly polarized (CP) light with nonzero orbital angular momentum (OAM)[23,24], can create vortex states in a two dimensional semiconductor.

More generally, it is intriguing to investigate whether the application of structured light, spatial[22,25,26] or spectral[27], can lead to interesting topological features, and which physical observables could reveal the properties of bulk, edge, and vortex states in such driven topological systems. For example, the frequency-dependence of the optical conductivity provides valuable information about charge carriers and elementary excitations in the dynamical responses. In particular, the real part of the dynamical Hall conductivity describes the reactive carrier response dynamics, and its imaginary part provides the dissipative response[28–42]. Additionally, orbital magnetization, defined by the magnetization arising from orbital motion of electrons, and its origin can yield an insightful picture about the electronic properties of the system[43–51]. The current density induced by OAM of light[52,53] has been proposed for further optical control of the magnetization in materials, enabling topological memory applications[54].

In this work, we evaluate the optical conductivity and orbital magnetization of a semiconductor driven with structured light, as proposed in[22]. To study the Hall conductivity, we employ a finite lattice derivation of dynamical conductivities via Kubo formalism[28,55–57], and we separate the contributions of different types of transitions determined by their initial and final states. This approach allows us to propose an experimental scheme to measure different contributions to the optical conductivity and to find the experimental signatures of vortex states as shown schematically in Fig. 1. Specifically, by tuning the chemical potential and the probe field frequency, we can measure the conductivity contribution arising only from the transition between two vortex states. By further tuning the frequency of the probe field, we can also measure other possible contributions from transitions between bulk, edge, and vortex states shown in Fig. 1c. Since the gap is set by the Rabi frequency, Ω_0, the relevant energy scale for bulk-bulk transition is Ω_0 while the energy difference between vortex-vortex and edge-edge is given by the light width and system size, respectively. For example, among different types of transitions, vortex-vortex and edge-edge transitions occur at lower probe frequencies compared to those required for the detection of the bulk-bulk contributions. The vortex-bulk and edge-bulk transitions need probe frequencies between these two frequency regimes.

Moreover, we study the orbital magnetization and current density of our Floquet system. We show that the current density induces nonzero orbital magnetization in the semiconductor. The orbital magnetization increases linearly with OAM of light, for both LP and CP light. Furthermore, we illustrate that the orbital magnetization density is independent of the Rabi frequency and light width. Finally, we demonstrate that in our setting, the orbital magnetization density is an intensive quantity because we assume that the light profile covers the entire system.

The orbital magnetization and current density induced by driving the system can be detected based on sensitive magnetometers, such as superconducting quantum interference devices (SQUIDs)[58] and nitrogen-vacancy (NV) centers[59–62]. We find that the CP light can create a rotating current density around the center of the light beam in a vortex state, while the density of current is localized along with the polarization of the LP light.

Results and discussion

Electronic Floquet vortex states of the driven system. In this section, we review our driven system Hamiltonian and the energy

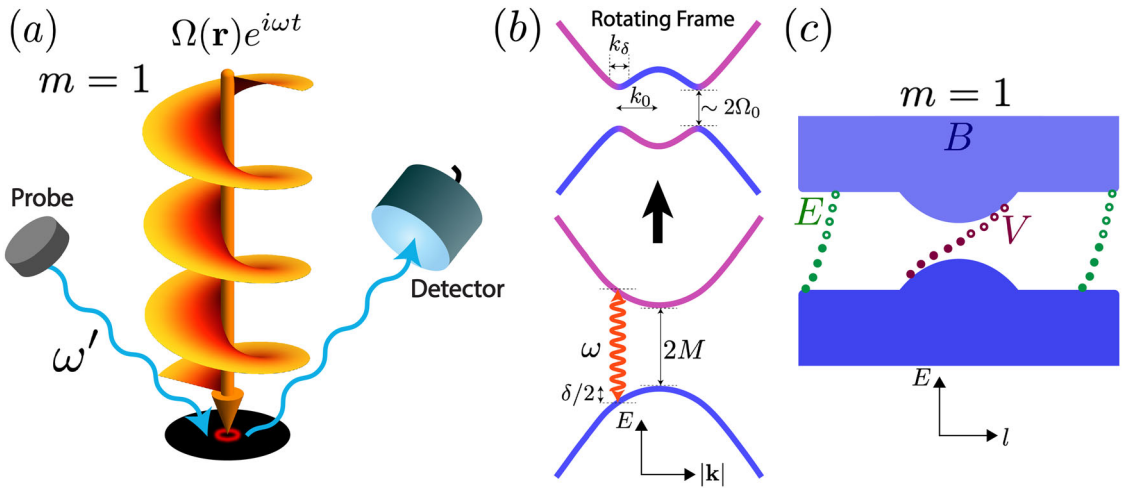

Fig. 1 Schematic of the driven two dimensional semiconductor system and energy dispersion of Floquet vortex states. a Schematic for the driven two dimensional (2D) semiconductor illuminated by light carrying orbital angular momentum with vorticity $m = 1$. The light beam's frequency is ω. This laser field opens up an energy gap in the rotating frame, while creating several midgap (vortex) states. The schematic profile of electrons in a vortex state is shown as the red circle around the light beam's center. Additionally, a setup for the measurement of longitudinal and Hall conductivity of the driven system using a probe field with frequency ω' and a detector to measure the conductivity is shown. **b** In the rotating frame, coupling the laser field with the semiconductor with gap $2M$ and detuning $\delta = \omega - 2M$, introduces the hybridization radius k_0 and the Floquet gap $2\Omega_0$ with the thickness k_δ. **c** The energy dispersion is plotted as a function of pseudo orbital angular momentum l as it becomes a good quantum number regarding the vorticity of light. The bulk, vortex, and edge states are shown in the blue area, red, and green dots, respectively.

spectrum. It is shown that shining light carrying nonzero OAM on a two dimensional semiconductor results in vortex states near resonant and weak field regimes[22]. Specifically, by considering a spinless massive Dirac 2D semiconductor described by the Hamiltonian $H_0 = (vk_x, vk_y, M)\cdot\sigma$, the rotating wave approximation (RWA) for the driven system by light with OAM can be applied. We set $\hbar = 1$ and $e = 1$ for all calculations, except when these parameters are explicitly determined. Here, M is half of the band gap and v is the Fermi velocity. A light beam with frequency ω which carries a nonzero OAM is shined on a semiconductor slab, as depicted in Fig. 1a, and its vector potential is denoted by $\mathcal{A}(\mathbf{r},t) = A_0(r)e^{im\phi}e^{i\omega t}\hat{\mathbf{x}} + \text{c.c.}$ We assume that the laser field satisfies the paraxial approximation, meaning that $A_0(r) = A_{\max}\left[1-\exp\{-r^2/(2\xi^2)\}\right]$ varies smoothly over the length scale of semiconductor lattice constant and of light width ξ. The radial part $A_0(r)e^{im\phi}$, where $r = \sqrt{x^2+y^2}$ and $\phi = \arctan(y/x)$, has integer vorticity m, representing the OAM of the laser field. Because of the vortex structure of the field, $A_0(r)$ vanishes at $r = 0$, for nonzero values of m. Since we assume that the semiconductor sample size is smaller than the beam size, this form of the vector potential is an approximation of the complete form of the Gaussian mode. As a result, the tail of the full vector potential is not included here and the amplitude of the field reaches to the constant value of $A_{\max}$ for $r >> \xi$. We note that this choice of vector potential violates the Coulomb gauge as $\hat{\mathbf{p}}.\mathcal{A} \neq \mathcal{A}.\hat{\mathbf{p}}$, where $\hat{\mathbf{p}} = (-i\partial_x, -i\partial_y)$ is the momentum operator. However, we can numerically show that the error is completely negligible, and the expectation values of the two terms $\hat{\mathbf{p}}.\mathcal{A}$ and $\mathcal{A}.\hat{\mathbf{p}}$ become even closer to each other as the system size R increases. The applied laser field hybridizes the valence and the conduction bands as it is shown in Fig. 1b, opening the energy gap around the resonance ring of momentum, $|\mathbf{k}| = k_0 = v^{-1}\sqrt{\omega^2/4 - M^2}$ where $\omega > 2M$ within the small detuning regime $\delta = \omega - 2M \ll \omega$. Starting with the minimal coupling, one can replace the wave vector $\mathbf{k}$ with $\mathbf{k} + e\mathcal{A}(\mathbf{r},t)$. To obtain the effective Hamiltonian from the time-periodic form $H(t) = H_0 + ev\mathcal{A}(\mathbf{r},t)\cdot\sigma$, we can use the RWA where we neglect fast oscillating terms in the time-dependent Floquet Hamiltonian, as an approximation method of the Floquet formalism, see Supplementary Note 1. As it is discussed in the Supplementary Notes 2 and 3 and shown with more details in reference[22], the final form of the Hamiltonian for the LP light reads as follows

$$H_{\text{RWA}} = \frac{\delta}{2}\left(\frac{\mathbf{k}^2}{k_0^2} - 1\right)\sigma_z + \left[\Omega(r)e^{-im\phi}\sigma_+ + \text{H.c.}\right] + O\left(\Omega_0\sqrt{\frac{\delta}{M}}\right), \tag{1}$$

where, $\Omega(\mathbf{r}) = evA(\mathbf{r})$ and $\Omega_0 = \lim_{r\to\infty}\Omega(\mathbf{r})$. We note that since we utilize a continuum Hamiltonian for the semiconductor, where the momentum corresponds to the large length scales in comparison to the lattice constant. Also, since the electric field is slowly varying over the lattice spacing, the wavevector $\mathbf{k}$ is replaced with the momentum operator $\hat{\mathbf{p}}$ in real space. After numerical diagonalization of the Hamiltonian, the dispersion of the Floquet system for the LP light with OAM can be acquired, as depicted in Fig. 2a for $m = 1$. The RWA Hamiltonian for the case of CP is derived in the Supplementary Note 3, and the corresponding energy dispersion is shown in Fig. 2b. As can be observed from Fig. 2, there are $|m|$ vortex state branches in the energy versus pseudo angular momentum diagram.

Based on the formalism followed in previous studies[22,63], here we present an estimation of the energy difference between subsequent vortex states. One can show that the energy

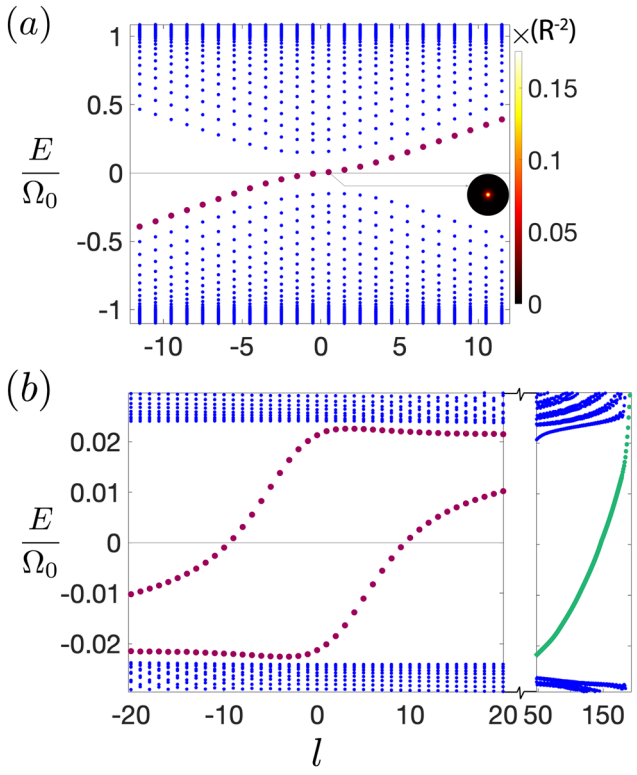

Fig. 2 Dispersion of energy versus pseudo orbital angular momentum for different vorticities m. a $m = 1$ of the linearly polarized light and **b** $m = 2$ of the circularly polarized light. We set $\omega = 2.05M$, $A_{\max} = 0.03M(ev)^{-1}$, $A_0(r) = A_{\max}[1-\exp\{-r^2/(2\xi^2)\}]$, and $\xi = 20k_\delta$. We use the disk sample radius $R = 10\xi$. As shown in these two examples, the number of vortex state branches can be determined by $|m|$. The bulk and vortex states are bolded in blue and red, respectively. For the circularly polarized light in **b**, edge states are colored in green. The spatial profile of electronic densities is shown in the inset of figure (**a**) with a color scale on the right-hand side.

separation between vortex states in the low-energy regime is given as follows

$$\omega_0 = \frac{\int_0^\infty \frac{\Omega(r)}{r} e^{-(2k_0/\delta)\int_0^r \Omega(r')dr'} dr}{k_0 \int_0^\infty e^{-(2k_0/\delta)\int_0^r \Omega(r')dr'} dr}. \tag{2}$$

We note that this physical quantity is system size-independent and determined solely by the bulk properties of the system and the radial profile of the irradiating beam. Therefore, its value remains constant in the thermodynamic limit. Here, we demonstrate how the energy difference between vortex states can be calculated based on properties of the shining light such as ω, δ, and Ω_0. By considering the following form for the radial beam profile

$$\Omega(r) = \begin{cases} \Omega_0(r/\xi)^q & \text{for } r \le \xi \\ \Omega_0 & \text{for } r > \xi \end{cases}, \; q \ge 1, \tag{3}$$

it can be shown that ω_0 can be approximated by the following expression

$$\omega_0 \simeq \Omega_0(k_0\xi)^{-1}(k_\delta\xi)^{-(q-1)/(q+1)}, \tag{4}$$

where $k_\delta \equiv k_0\Omega_0/\delta$. Therefore, the energy separations ω_0 depend on the applied light beam properties such as its frequency ω, and the radial profile including parameters ξ for the light width, Ω_0 for the intensity, and q for the light shape. From the approximate energy separation between subsequent vortex states, we can

estimate the number of vortex states in one branch as follows

$$2\Omega_0/\omega_0 \simeq k_0\xi(k_\delta\xi)^{(q-1)/(q+1)}. \quad (5)$$

For $q \geq 1$, one can further simplify this estimation by determining the lower bound of $2\Omega_0/\omega_0 \simeq k_0\xi$. Since we are in the small detuning regime $\xi^{-1} \ll k_0 \ll M/\nu$, there are many vortex states in a vortex branch as $2\Omega_0/\omega_0 \gg 1$.

Optical conductivity. Here, the optical conductivity of the system described in the previous section is calculated. With the obtained wave functions in the form of Bessel functions and energy spectrum, we can calculate the longitudinal and Hall optical conductivities via Kubo formalism in the real space configuration in polar coordinates. To measure the dynamical conductivity, we apply a weak, linearly polarized alternating current (AC) probe field that is normal to the surface of the semiconductor, as it is shown schematically in Fig. 1a. Here, we review the real space expression for the dynamical conductivity. We note that, due to the vortex structure of the laser field, the translational symmetry is explicitly broken, and all the calculations of Hall and longitudinal conductivities should be performed on a disc with finite radius R. We assume that the non-perturbed time-independent Hamiltonian is labeled by H_0. We consider a time-dependent perturbation $H = H_0 + H'(t)$ and apply the Liouville-von Neumann equation $i\hbar\partial_t\rho = [H, \rho]$ for the density matrix $\rho = \rho_0 + \delta\rho$ in the linear response regime. Relations $H_0|\alpha\rangle = \epsilon_\alpha|\alpha\rangle$, $\rho_0|\alpha\rangle = n_\alpha(\epsilon)|\alpha\rangle$ can be used in Liouville-von Neumann equation, where n_α is the Fermi-Dirac distribution. In other words, we assume that the system is thermalized in the rotating frame. With the assumption of periodic time dependence of $H'(t) \propto e^{i\omega' t}$, we have $\hbar\omega'\delta\rho = [H', \rho_0] + [H_0, \delta\rho]$, where ω' is the frequency of the prob field. Thus the components of $\delta\rho$ can be obtained as follows

$$\langle\beta|\delta\rho|\alpha\rangle = \frac{(n_\beta - n_\alpha)\langle\beta|H'|\alpha\rangle}{(\epsilon_\beta - \epsilon_\alpha) - \hbar\omega' - i\eta}, \quad (6)$$

where η is the quasiparticle lifetime broadening, $\alpha(\beta)$ is a collective label for the relevant quantum state including the band index n, pseudo-OAM l, and the type of the state from the set {bulk, vortex, edge}.

We can rewrite the perturbation in terms of velocity operator given by $H' = eA^\mu_p p_\mu/m = ev_\mu E_\mu/(i\omega')$, where $\mu, \nu \in \{x, y\}$, $e > 0$ is the elementary charge and Einstein summation rule is applied. Employing the Heisenberg equation of motion for time-dependent perturbations, one obtains $\langle\beta|v_\mu|\alpha\rangle = \langle\beta|[x_\mu, H]|\alpha\rangle/(i\hbar) \approx \langle\beta|x_\mu|\alpha\rangle(\epsilon_\alpha - \epsilon_\beta)/(i\hbar)$. The single particle current density operator is defined as $j_\mu = \frac{1}{S}\frac{\delta H}{\delta A^\mu_p(\mathbf{r})} = (-e)v_\mu/S$, where S is the area of the two-dimensional system (here, $S = \pi R^2$). By substituting the previous relations into the average current density defined by the following equation, we get

$$\begin{aligned} J_\mu &= Tr[j_\mu\delta\rho] = \sum_{\alpha\beta}\langle\beta|\delta\rho|\alpha\rangle\langle\alpha|j_\mu|\beta\rangle \\ &= -\frac{2\pi\sigma_0}{Sh}\sum_{\alpha\beta}\frac{(n_\beta - n_\alpha)\epsilon^2_{\beta\alpha}}{\epsilon_{\beta\alpha} - \hbar\omega' - i\eta}\langle\alpha|x_\mu|\beta\rangle\langle\beta|x_\nu|\alpha\rangle A_\nu, \end{aligned} \quad (7)$$

where $\epsilon_{\beta\alpha} \equiv \epsilon_\beta - \epsilon_\alpha$ is the energy difference between final (β) and initial (α) transition states and $\sigma_0 \equiv e^2/h$ is the quantum of conductance. The paramagnetic current correlation function $\Pi^{\mu\nu}(\omega')$ is defined by the equation $J_\mu = \Pi^{\mu\nu}(\omega')A_\nu$. Therefore, the following final equation for the dynamical conductivity can be acquired

$$\begin{aligned} \sigma_{\mu\nu}(\omega') &= \frac{\Pi^{\mu\nu}(\omega') - \Pi^{\mu\nu}(0)}{i\omega'} \\ &= \frac{2\pi i\sigma_0}{Sh}\sum_{\alpha\beta}\frac{(n_\beta - n_\alpha)\epsilon_{\beta\alpha}}{\tilde{\epsilon}_{\beta\alpha} - \omega' - i\eta}\langle\alpha|x_\mu|\beta\rangle\langle\beta|x_\nu|\alpha\rangle. \end{aligned} \quad (8)$$

We set $\eta = 9.6 \times 10^{-6}$ and $\eta = 5.6 \times 10^{-7}$ for irradiating LP and CP light carrying OAM, respectively. The reason we need to use different values for η is due to the different Hamiltonian energy scales for the LP and CP cases as shown in Eq. (1) and Supplementary Eq. (14). We should note that while our initial steps in derivation of Eq. (8) are similar to the reference[64], our final expression that we use in our simulation is different. The matrix elements in Eq. (8) capture the transition processes among the bulk, edge, and vortex states. There are five types of transitions, i.e., edge-to-edge (E-E), edge-to-bulk (E-B), vortex-to-vortex (V-V), vortex-to-bulk (V-B), and bulk-to-bulk (B-B). In the system, the V-E transition is not possible because vortex and edge states' branches are located in separate ranges of pseudo-OAM l in the dispersion, sufficiently far from each other so that the transition rule, $l' = l \pm 1$, cannot be obeyed. Using the wave functions' expressions in Supplementary Eq. (9), we obtain the following matrix form with corresponding transition rules for various contributions. We note that the transition rules $l = l' \pm 1$ are obtained by integrating the angular part of terms $\langle\alpha|x_\mu|\beta\rangle$

$$\begin{aligned} \langle\psi^{S'}_{l'n'}|\hat{x}|\psi^{S}_{ln}\rangle &= \mathcal{T}^{S'S}_{l'n',ln}(\delta_{l,l'+1} + \delta_{l,l'-1}) \\ \langle\psi^{S'}_{l'n'}|\hat{y}|\psi^{S}_{ln}\rangle &= \mathcal{T}^{S'S}_{l'n',ln}(i\delta_{l,l'+1} - i\delta_{l,l'-1}), \end{aligned} \quad (9)$$

where, $\delta_{l,l'}$ is the Kronecker delta symbol, $S', S \in \{B, E, V\}$ represent the bulk, edge, and vortex states, and $\mathcal{T}^{S'S}_{l'n',ln}$ is a dimensionless radial integration part derived by

$$\mathcal{T}^{S'S}_{l'n',ln} = \int_0^R dr r^2(u_{n,l,+}(r)u_{n',l',+}(r) + u_{n,l,-}(r)u_{n',l',-}(r)). \quad (10)$$

In Figs. 3 and 4, different contributions of the optical conductivity (Hall and longitudinal) for LP and CP light beams are shown, respectively. Figure 3a illustrates the electronic transfer among different types of states that includes V-V, V-B, E-E, E-B, and B-B transitions, which are shown in red, gray, green, orange, and blue, respectively. According to the transition rule obtained in the Kubo formalism in Eq. (9), it can be seen that V-V transition occurs only between a state below and a state above the Fermi level. Thus, there is only one resonance peak in $m = 1$ for V-V in Fig. 3b, c, corresponding to the energy difference between two subsequent vortex states that can be approximated by ω_0 as expressed in Eq. (2). We also note that since the two vortex states at zero energy are particle-hole symmetric to each other as we showed below Supplementary Eq. (10), the radial parts of their wave functions cancel each other out. As a result, the intensity of the V-V transition at zero energy vanishes. Therefore, we need to change the chemical potential to select two vortex states far from the zero energy so that the transition between two subsequent vortex states becomes nonzero. Despite the behavior of V-V transitions for $m = 1$, there are many peaks in the V-B contributions. In Fig. 3b, c, the V-B has several peaks because of several transitions between vortex states in the gap and possible bulk states, corresponding to transition frequencies between these states which for our parameters is around the energy $\omega' \sim \Omega_0/4$. The B-B contribution has even more peaks in comparison to the case of V-B since the bulk transitions scale with the system's area. The location of peaks covers energy differences in the range $2\Omega_0 < \omega'$ and decays for higher probe frequencies.

The V-V transition for the light beam carrying OAM with CP shown in Fig. 4a, b, has very similar behavior to the LP light,

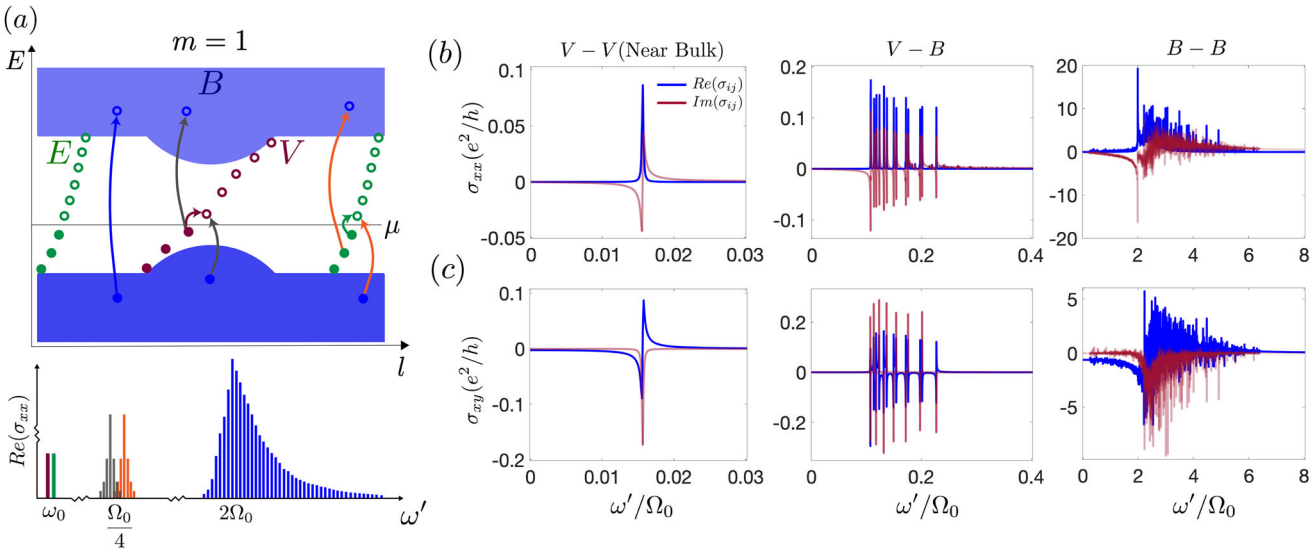

Fig. 3 Optical conductivity of Floquet vortex states for the linearly polarized light. a Schematic of energy dispersion illustrating that tuning the probe field frequency through different regimes can measure different optical conductivity contributions. The bulk, vortex, and edge states are shown in blue areas, red, and green dots, respectively. Three contributions vortex-vortex (V-V), vortex-bulk (V-B), and bulk-bulk (B-B) can be considered for the Hall and longitudinal conductivities of linearly polarized light. In addition, two more contributions edge-edge (E-E) and edge-bulk (E-B) are also possible for the circularly polarized light. The vortex-vortex, vortex-bulk, edge-edge, edge-bulk, and bulk-bulk transitions are shown in red, gray, green, orange, and blue arrows, respectively. The corresponding location of each type of transition for $Re(\sigma_{xx})$ is shown below schematically, for a system driven by linearly polarized light. **b** Numerical results for the longitudinal and **c** the Hall conductivity of linearly polarized light σ_{xy} and σ_{xx}, versus probe frequency ω' for contributions from different types of transitions. Parameters here are the same as shown in Fig. 2 and the vorticity of light is $m = 1$. Blue and red lines correspond to the real and imaginary parts of conductivity, respectively.

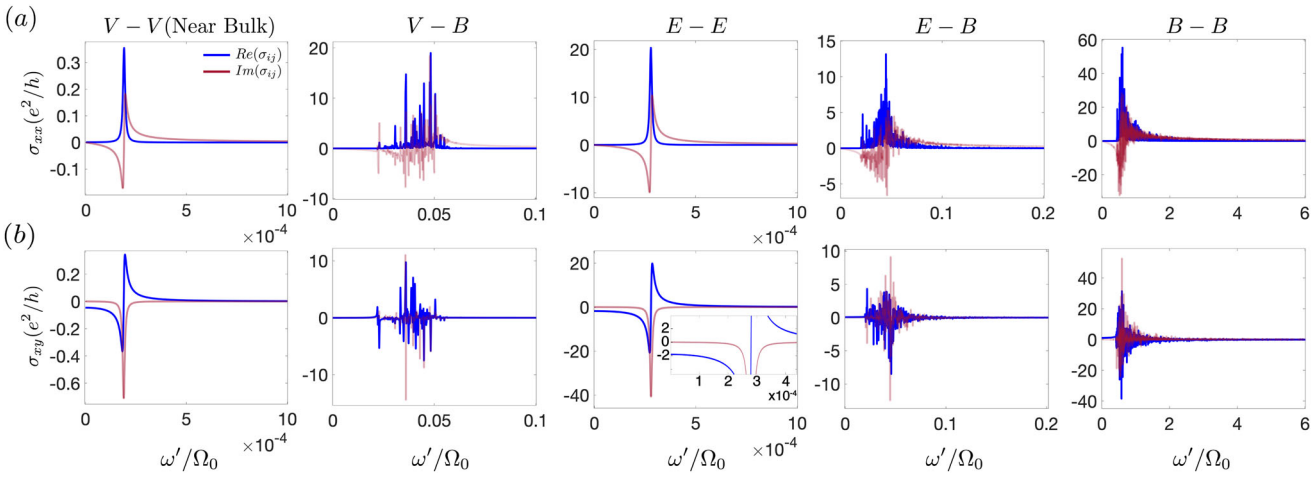

Fig. 4 Optical conductivity of Floquet system driven by the circularly polarized light. The optical conductivities, **a** Hall (σ_{xy}) and **b** longitudinal (σ_{xx}), for circularly polarized light, versus probe frequency ω' and vorticity $m = 1$ for different types of transitions. The Hall conductance at zero frequency is shown in the inset of the edge-edge panel in (**b**). Parameters are the same as in Fig. 2. Blue and red lines indicate the real and imaginary parts of optical conductivity, respectively.

where the peaks for $\sigma_{xx/xy}$ occur at resonance with the energy difference between two vortex states, ω_0. We note that energy scales for CP light are smaller than LP light by a factor of $v^2(2M)^{-1}$ as it is demonstrated in the Hamiltonian in Supplementary Eq. (14). As can be observed from Fig. 4, in the case of CP light, the E-E contribution to the Hall conductivity is dominant. The E-E contribution reaches the value ~1.95 as $\omega' \to 0$, corresponding to the quantized Hall conductance, according to the existing two chiral edge modes and Chern number two for topological Floquet insulator. In the E-B contribution of CP light, similar to the case of LP light, there are more possible transitions than the cases of V-V and E-E as shown in Fig. 4. The V-B transition for the LP light shown in Fig. 3 has distinct peaks because of the more separate vortex states (larger ω_0) in the gap of the driven system in comparison to the case of CP light. The B-B transition for CP illumination has more resonance peaks than all other transition types. Similarly, the reason is that more possible electron transfers obeying transition rules between bulk states are available in comparison to other contributions. For the CP light, most B-B peaks occur around frequency range $v^4\Omega_0(2M)^{-1} < \omega'$ and decay exponentially at higher frequencies. Different types of transitions are also discussed for the OAM of light $m = 2$ for the LP light in the Supplementary Note 4 and Supplementary Fig. 1. Most of the

contributions are very similar to the case of $m=1$, except the V-V transition for vorticity $m=2$ has more peaks for electron transfer between vortex states. This is because, for $m=2$, transitions between vortex branches are also possible and introduce more peaks as it is depicted in the Supplementary Fig. 1.

We note that it is not possible to measure the optical conductivity of vortex states locally. This is because the wavelength of the probe field for V-V transition is of the order of $\lambda \sim \frac{1}{\omega_0} \gg R$, and thus larger than the radius of localized electronic density in a vortex state that is located around the center of the light as shown schematically in Fig. 1a.

However, we can show that it is possible to distinguish transitions between different types of states spectrally. To separate different contributions of conductivity in experiments, one can use the optical conductivity measurements by tuning the probe field frequency properly. To detect vortex states and measure their contributions to the dynamical conductivity, the chemical potential should be tuned to be in the bulk gap of the driven system and not exactly at energy zero. The reason for the latter condition is because of the vanishing amplitude of the transitions between vortex states above and below the energy zero as their radial integration in Eq. (10) vanishes. By tuning the probe field frequency ω' to be less than the bulk gap, one can remove any bulk contributions as shown by the red transition in Fig. 3a. Then to measure the B-V contribution, the probe frequency can be tuned to include B-V contributions as illustrated in Fig. 3a in gray transition. After measuring the contribution of V-V and V-B, by choosing the probe frequency to be equal to or higher than the bulk gap, B-B contribution can be possible and measured as shown with blue transition in Fig. 3a. We note that the amplitudes of V-V transitions are system size-dependent and they decrease as the radius of the system, R, increases. However, here we use this finite-size effect to acquire the signature of the vortex states in the optical conductivity. We can also tune Rabi frequency Ω_0 and light width ξ to change the intensity of optical conductivity. The optical conductivity can increase as a function of light width and decrease when the Rabi frequency increases, as shown in Fig. 5a, b, respectively.

To verify the experimental feasibility of the optical conductivity measurements in our system, we note that realizing our Floquet system, similar to other recent studies[14,15], requires strong laser fields. While so far the experiments have been performed on gapped states, we use their numbers as a guide for our proposal in semiconductors. The intense fields pump a considerable amount of energy into the system, and therefore can quickly heat the system. Therefore, in such settings where states of the driven Hamiltonian have been shown to survive for around 1ps, our proposed vortex states can be created transiently. Correspondingly, to measure the physical signatures of these states, one needs to consider an ultrafast measurement protocol. The typical vector potential and detuning that we have assumed in our proposal are $A_0 = 0.015M(ev)^{-1}$ and $\delta = 0.1M$. This value corresponds to the Rabi frequency $\Omega_0 = evA_0 = 3.6$ THz for a semiconductor band gap $M \sim 1$ eV and Fermi velocity $v \sim 10^5\,\mathrm{ms}^{-1}$. The corresponding intensity for such a Rabi frequency is $I = \frac{c\epsilon_0}{2}\omega^2 A^2 = 2.1\times 10^{12}\,\mathrm{Wm}^{-2}$ which is close to the intensity used in ref. [15], where c is the speed of light and ϵ_0 is the dielectric permittivity of vacuum. Based on Figs. 3 and 4, optical conductivity peaks in our system occur in the range of probe frequencies $\omega' \sim \frac{1}{100}\Omega_0$ to $\omega' \sim \Omega_0$. Here, the inverse of the probe frequency can be compared with the duration of the recent ultrafast DC measurement of anomalous Hall conductivity in the driven graphene[15]. The inverse of probe frequencies in optical conductivity can be within the range of 30–1000 fs and are less than the duration of such experiments. Therefore, we conclude that our measurement scheme for the optical conductivity of different types of transitions is experimentally achievable.

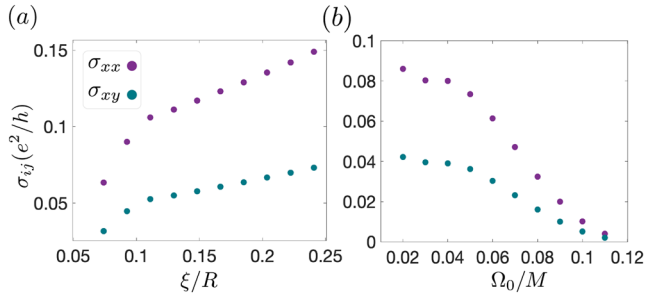

Fig. 5 Tuning of optical conductivity by light width and Rabi frequency. **a** Optical conductivity as a function of light width ξ, and **b** as a function of Rabi frequency Ω_0 for vortex-vortex transition of linearly polarized light as it is depicted in Fig. 3c.

Orbital magnetization and current density. To further understand the effect of the vorticity of light on the electronic system, we calculate the electronic current density and orbital magnetization. Here, for the wave functions of the quantum states, $\psi(\mathbf{r}) = \langle \mathbf{r}|\psi_{m,\mathbf{k}}\rangle$, the current density is given by

$$\mathbf{j}(\mathbf{r}) = -e\psi^{\dagger}(\mathbf{r})\frac{\partial H_{RWA}}{\partial \mathbf{k}}\psi(\mathbf{r}). \tag{11}$$

As shown in Fig. 6a, the current density of a vortex state is highly localized around the center of the light carrying nonzero OAM for both LP and CP laser fields. In the case of linear polarization, the current density is aligned linearly along the polarization of the light beam. The width of this localization increases as ξ increases and as we select the vortex states far from the zero energy as shown in Fig. 6b. The rotation of the current density for the CP case is detected by the handedness of the beam. Then, we calculate the orbital magnetization of occupied states in the presence of vortex states for different vorticities m. The orbital magnetization is defined as follows

$$\mathbf{m} = -\frac{e}{2}\sum_{\epsilon_i<\mu}\langle\psi_i|\mathbf{r}\times\mathbf{v}|\psi_i\rangle, \tag{12}$$

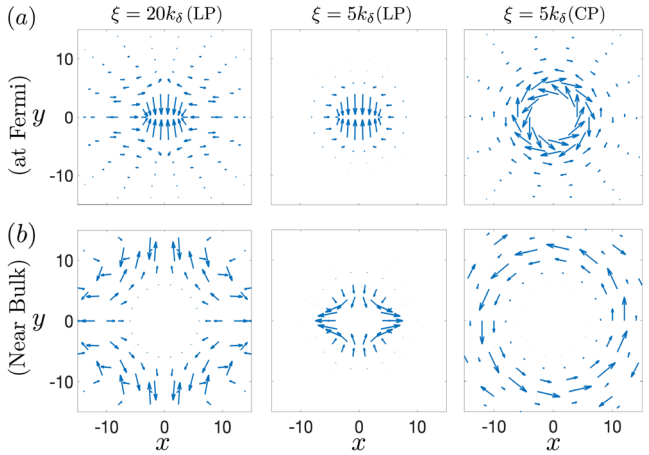

Fig. 6 Current density induced by light carrying orbital angular momentum. **a** Current density of vortex states, demonstrating highly localized current density around the center of light for the vortex states closest to the zero energy. **b** Current densities for the vortex states far from the zero energy and near the bulk states. Parameters for both **a** and **b** are the same as Fig. 2, except ξ that is determined here separately.

where summation is over occupied states, $\mathbf{v} = -\frac{i}{\hbar}[\mathbf{r}, H]$ and the disc area $S = \pi R^2$ for $\mathbf{r} = (\hat{x}, \hat{y}, \hat{z})$. Since our low momentum Floquet theory captures the physics only around the early Dirac point in the semiconductor, we always set chemical potential $\mu = 0$ when calculating the orbital magnetization. One can write the following expression

$$\mathcal{M}_z = \frac{ie}{2S\hbar} \sum_{\epsilon_i < \mu} \langle \psi_i | (\hat{x}[\hat{y}, H] - \hat{y}[\hat{x}, H]) | \psi_i \rangle. \quad (13)$$

The averaged magnetization density $\mathcal{M}_z$ can then be defined as the magnetic moment $\mathbf{m}$ per unit area for a 2D system along the z-direction. As shown in Fig. 7, the averaged magnetization density increases linearly as a function of light vorticity m for both LP and CP cases. Therefore, the orbital magnetization density is zero for $m = 0$ for the LP light. However, there is a remaining magnetization of CP light for vorticity $m = 0$ that results from states hosting circular current density and nonzero magnetic moments. We note that the circular current density can also be observed among bulk and edge states in the case of CP light. Additionally, the averaged orbital magnetization density for the system is independent of the Rabi frequency of light Ω_0, the width of light carrying OAM ξ, and the disc's radius R (an intensive quantity) as demonstrated in Fig. 8a, b, and c, respectively. It should be noted that while Fig. 8c shows the entire range for R, small disc radii in the range $R \lesssim 5\xi$ are not physical. The value of ξ is limited by the lower bound of $\lambda/2$, where λ is the wavelength of the light. Therefore, for the semiconductor with a gap of 1eV, the ξ has the typical value of 1 micron. As a result, the minimum value of the sample size R is around 10 microns. We note that the independence of the magnetization results from the Rabi frequency may at first seem counter-intuitive, especially from the point of view of a driven two-level system. However, upon further scrutiny, it turns out that such behavior is acceptable within our model. The underlying reason is that in evaluating the magnetization, to simplify our calculations, we have assumed a nearly zero-temperature occupation of the Floquet bands corresponding to a full occupation of the Floquet valence band[65]. However, in a typical experimental setting, the dissipative electron-phonon interactions tend to relax the distribution of the electrons from the undriven conduction band to the valence band, so that the occupation probability of electrons in the Floquet valence band around the resonance surface could be significantly lower than one and is controlled by the Rabi frequency[5,34]. Therefore, our model assumes that the occupation of the bands is insensitive to the Rabi frequency, the resulting magnetization tends to be independent of the Rabi frequency.

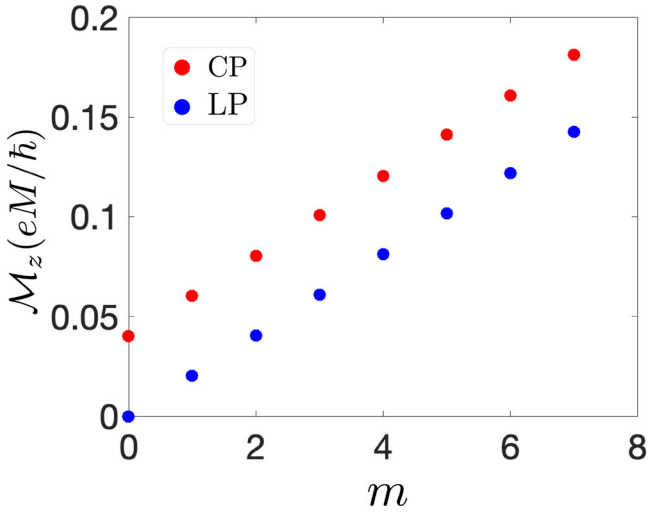

Fig. 7 Orbital magnetization of the Floquet system. Orbital magnetization of the Floquet system, indicating a linear increase in the diagram of orbital magnetization as a function of m for both circularly polarized and linearly polarized laser fields. The same set of parameters as in Fig. 2 are used here.

From a semiclassical point of view, electronic magnetization is determined by the angular speed of electrons. Therefore, based on our results, we can deduce that the effective angular speed of electrons in our system is proportional to the vorticity of the light, and is independent of the Rabi frequency and width of the light. For the same semiconductor parameters described in the last paragraph of the optical conductivity section and the sample radius of $R = 10\,\mu m$, the typical evaluated magnetization $\mathcal{M}_z = 0.1(eM\hbar^{-1})$ yield a total magnetic moment of $\mu = \mathcal{M}_z \times \pi R^2 \simeq 10^9\ \mu_B$ in terms of Bohr magneton. Such a magnetic moment can be probed by sensitive SQUID scanning microscopy measurements[58]. The nonzero magnetization indicates the existence of nonzero current densities as some examples are calculated in Fig. 6. To measure the magnetization spatially with a nano-scale resolution, one can use the magnetometry based on nitrogen-vacancy (NV) centers in the diamond[59–62]. Other possible experimental schemes to study the magnetization are magneto-optical measurements of Kerr rotation and Faraday effects[66,67] and circular dichroism in angle-resolved photoemission spectroscopy (ARPES) measurements[68–70]. However, since our Floquet system can only be realized transiently, ultrafast measurement devices that can measure transient magnetic signals are required. We also note that the energy of vortex states can be visible by ARPES measurements as this method can acquire the energy dispersion of the system[13,14].

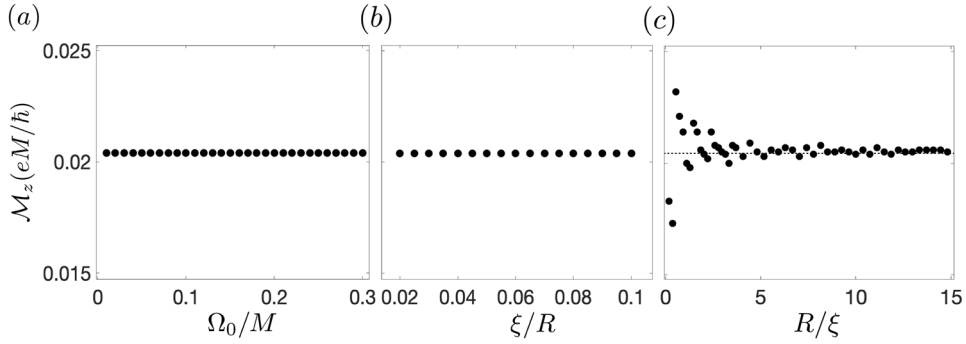

Fig. 8 The dependence of orbital magnetization on system parameters. The independence of orbital magnetization density as a function of **a** Rabi frequency, Ω_0, **b** the light width, ξ, while keeping the system size R constant, and **c** disc radius R, where the light width ξ is constant. The same parameters as in Fig. 2 are used here, except the one that is changed in this figure.

Regarding the applicability of a low-momentum treatment of the Hall conductivity and the magnetization, we note that because of the structured profile of the light, the translational symmetry is broken, and we only can sum over states that are being created from our low momentum theory. Therefore, our results for the magnetization depend on the pseudo-OAM cutoff of the dispersion (l_c), albeit weakly. As a result, the magnetization calculated here can represent only the order of magnitude of the magnetization in the Floquet system instead of its exact values. However, since generally, in the presence of translational symmetry, the magnetization density depends on the momentum derivatives of the wave functions[71], we expect that for our system, the main contribution to the magnetization density should be attributable to the region in the vicinity of the Dirac points where the curvature of the bands is significant, and we expect it to be captured by our low-momentum theory. In particular, in[72] it is demonstrated that in a gapped graphene system, only momenta around the Dirac points K and K' contribute to the magnetization. Therefore, this assumption that our low momentum theory calculates the main part of the magnetization should be valid.

Conclusions

In this study, two physical observables – optical conductivity and orbital magnetization – of the Floquet system driven by a structured light carrying nonzero OAM are calculated. While we only considered the modification of the electronic band structure from the OAM light beam, it is a stepping stone to adding electronic interactions in the system which may realize novel many-body states. In particular, the possibility of creating exotic states in the presence of non-equilibrium superconducting phases in semimetals, semiconductors, and strongly correlated materials[73–78] could be subjects of future research. Another aspect of our proposal that needs further investigation is the study of thermodynamic effects. In particular, while here we have assumed that our driven system has thermalized in the driven frame such that only the ground state in the rotating frame is occupied, in general creating such a distribution requires system-bath engineering techniques. Such methods have been studied in the presence of electron-phonon interactions[5,34,65,79] and applying these methods to our proposal could be the subject of future studies.

Data availability

The data that support the findings of this study are available from the corresponding author upon reasonable request.

Received: 19 July 2022; Accepted: 12 June 2023;
Published online: 23 June 2023

References

1. Oka, T. & Aoki, H. Photovoltaic hall effect in graphene. *Phys. Rev. B* **79**, 081406 (2009).
2. Kitagawa, T., Berg, E., Rudner, M. & Demler, E. Topological characterization of periodically driven quantum systems. *Phys. Rev. B* **82**, 235114 (2010).
3. Lindner, N. H., Refael, G. & Galitski, V. Floquet topological insulator in semiconductor quantum wells. *Nat. Phys.* **7**, 490–495 (2011).
4. Goldman, N. & Dalibard, J. Periodically driven quantum systems: effective hamiltonians and engineered gauge fields. *Phys. Rev. X* **4**, 031027 (2014).
5. Dehghani, H., Oka, T. & Mitra, A. Dissipative floquet topological systems. *Phys. Rev. B* **90**, 195429 (2014).
6. Sato, S. A. et al. Microscopic theory for the light-induced anomalous hall effect in graphene. *Phys. Rev. B* **99**, 214302 (2019).
7. Tancogne-Dejean, N., Sentef, M. A. & Rubio, A. Ultrafast modification of hubbard *u* in a strongly correlated material: Ab initio high-harmonic generation in nio. *Phys. Rev. Lett.* **121**, 097402 (2018).
8. Titum, P., Berg, E., Rudner, M. S., Refael, G. & Lindner, N. H. Anomalous floquet-anderson insulator as a nonadiabatic quantized charge pump. *Phys. Rev. X* **6**, 021013 (2016).
9. Quinteiro Rosen, G. F., Tamborenea, P. I. & Kuhn, T. Interplay between optical vortices and condensed matter. *Rev. Mod. Phys.* **94**, 035003 (2022).
10. Li, J. et al. Electromagnetic coupling in tight-binding models for strongly correlated light and matter. *Phys. Rev. B* **101**, 205140 (2020).
11. Dmytruk, O. & Schiró, M. Gauge fixing for strongly correlated electrons coupled to quantum light. *Phys. Rev. B* **103**, 075131 (2021).
12. Di Stefano, O. et al. Resolution of gauge ambiguities in ultrastrong-coupling cavity quantum electrodynamics. *Nat. Phys.* **15**, 803–808 (2019).
13. Wang, Y. H., Steinberg, H., Jarillo-Herrero, P. & Gedik, N. Observation of floquet-bloch states on the surface of a topological insulator. *Science* **342**, 453–457 (2013).
14. Mahmood, F. et al. Selective scattering between floquet–bloch and volkov states in a topological insulator. *Nat. Phys.* **12**, 306–310 (2016).
15. McIver, J. W. et al. Light-induced anomalous hall effect in graphene. *Nat. Phys.* **16**, 38–41 (2020).
16. Zupancic, P. et al. Ultra-precise holographic beam shaping for microscopic quantum control. *Opt. Express* **24**, 13881–13893 (2016).
17. Barredo, D., de Léséleuc, S., Lienhard, V., Lahaye, T. & Browaeys, A. An atom-by-atom assembler of defect-free arbitrary two-dimensional atomic arrays. *Science* **354**, 1021–1023 (2016).
18. Bernien, H. et al. Probing many-body dynamics on a 51-atom quantum simulator. *Nature* **551**, 579–584 (2017).
19. Schine, N., Chalupnik, M., Can, T., Gromov, A. & Simon, J. Electromagnetic and gravitational responses of photonic landau levels. *Nature* **565**, 173–179 (2019).
20. Yan, Y. et al. High-capacity millimetre-wave communications with orbital angular momentum multiplexing. *Nat. Commun.* **5**, 1–9 (2014).
21. Gariepy, G. et al. Creating high-harmonic beams with controlled orbital angular momentum. *Phys. Rev. Lett.* **113**, 153901 (2014).
22. Kim, H., Dehghani, H., Ahmadabadi, I., Martin, I. & Hafezi, M. Floquet vortex states induced by light carrying an orbital angular momentum. *Phys. Rev. B* **105**, L081301 (2022).
23. Allen, L., Beijersbergen, M. W., Spreeuw, R. J. C. & Woerdman, J. P. Orbital angular momentum of light and the transformation of laguerre-gaussian laser modes. *Phys. Rev. A* **45**, 8185–8189 (1992).
24. Yao, A. M. & Padgett, M. J. Orbital angular momentum: origins, behavior and applications. *Adv. Opt. Photon.* **3**, 161–204 (2011).
25. Katan, Y. T. & Podolsky, D. Modulated floquet topological insulators. *Phys. Rev. Lett.* **110**, 016802 (2013).
26. Kim, H., Dehghani, H., Aoki, H., Martin, I. & Hafezi, M. Optical imprinting of superlattices in two-dimensional materials. *Phys. Rev. Res.* **2**, 043004 (2020).
27. Castro, A., De Giovannini, U., Sato, S. A., Hübener, H. & Rubio, A. Floquet engineering the band structure of materials with optimal control theory. *Phys. Rev. Res.* **4**, 033213 (2022).
28. Maciejko, J., Qi, X.-L., Drew, H. D. & Zhang, S.-C. Topological quantization in units of the fine structure constant. *Phys. Rev. Lett.* **105**, 166803 (2010).
29. Wu, L. et al. Quantized faraday and kerr rotation and axion electrodynamics of a 3d topological insulator. *Science* **354**, 1124–1127 (2016).
30. Okada, K. N. et al. Terahertz spectroscopy on faraday and kerr rotations in a quantum anomalous hall state. *Nat. Commun.* **7**, 12245 (2016).
31. Dehghani, H., Oka, T. & Mitra, A. Out-of-equilibrium electrons and the hall conductance of a floquet topological insulator. *Phys. Rev. B* **91**, 155422 (2015).
32. Dehghani, H. & Mitra, A. Optical hall conductivity of a floquet topological insulator. *Phys. Rev. B* **92**, 165111 (2015).
33. Dehghani, H. & Mitra, A. Occupation probabilities and current densities of bulk and edge states of a floquet topological insulator. *Phys. Rev. B* **93**, 205437 (2016).
34. Dehghani, H. & Mitra, A. Floquet topological systems in the vicinity of band crossings: reservoir-induced coherence and steady-state entropy production. *Phys. Rev. B* **93**, 245416 (2016).
35. Nuske, M. et al. Floquet dynamics in light-driven solids. *Phys. Rev. Res.* **2**, 043408 (2020).
36. Mak, K. F. et al. Measurement of the optical conductivity of graphene. *Phys. Rev. Lett.* **101**, 196405 (2008).
37. Morimoto, T., Hatsugai, Y. & Aoki, H. Optical hall conductivity in ordinary and graphene quantum hall systems. *Phys. Rev. Lett.* **103**, 116803 (2009).
38. Ikebe, Y. et al. Optical hall effect in the integer quantum hall regime. *Phys. Rev. Lett.* **104**, 256802 (2010).
39. Qi, X.-L., Li, R., Zang, J. & Zhang, S.-C. Inducing a magnetic monopole with topological surface states. *Science* **323**, 1184–1187 (2009).
40. Rokaj, V., Penz, M., Sentef, M. A., Ruggenthaler, M. & Rubio, A. Polaritonic hofstadter butterfly and cavity control of the quantized hall conductance. *Phys. Rev. B* **105**, 205424 (2022).
41. Topp, G. E. et al. Topological floquet engineering of twisted bilayer graphene. *Phys. Rev. Res.* **1**, 023031 (2019).

42. Foa Torres, L. E. F., Perez-Piskunow, P. M., Balseiro, C. A. & Usaj, G. Multiterminal conductance of a floquet topological insulator. *Phys. Rev. Lett.* **113**, 266801 (2014).
43. Topp, G. E., Törmä, P., Kennes, D. M. & Mitra, A. Orbital magnetization of floquet topological systems. *Phys. Rev. B* **105**, 195426 (2022).
44. Nathan, F., Rudner, M. S., Lindner, N. H., Berg, E. & Refael, G. Quantized magnetization density in periodically driven systems. *Phys. Rev. Lett.* **119**, 186801 (2017).
45. Dahlhaus, J. P., Fregoso, B. M. & Moore, J. E. Magnetization signatures of light-induced quantum hall edge states. *Phys. Rev. Lett.* **114**, 246802 (2015).
46. Souza, I. & Vanderbilt, D. Dichroic *f*-sum rule and the orbital magnetization of crystals. *Phys. Rev. B* **77**, 054438 (2008).
47. Bianco, R. & Resta, R. Orbital magnetization in insulators: bulk versus surface. *Phys. Rev. B* **93**, 174417 (2016).
48. Thonhauser, T., Ceresoli, D., Vanderbilt, D. & Resta, R. Orbital magnetization in periodic insulators. *Phys. Rev. Lett.* **95**, 137205 (2005).
49. Hara, D., Bahramy, M. S. & Murakami, S. Current-induced orbital magnetization in systems without inversion symmetry. *Phys. Rev. B* **102**, 184404 (2020).
50. Bianco, R. & Resta, R. Orbital magnetization as a local property. *Phys. Rev. Lett.* **110**, 087202 (2013).
51. Boström, E. V. et al. All-optical generation of antiferromagnetic magnon currents via the magnon circular photogalvanic effect. *Phys. Rev. B* **104**, L100404 (2021).
52. Wätzel, J. & Berakdar, J. Centrifugal photovoltaic and photogalvanic effects driven by structured light. *Sci. Rep.* **6**, 1–7 (2016).
53. Quinteiro, G. F. & Tamborenea, P. I. Twisted-light-induced optical transitions in semiconductors: free-carrier quantum kinetics. *Phys. Rev. B* **82**, 125207 (2010).
54. Pershoguba, S. S. & Yakovenko, V. M. Optical control of topological memory based on orbital magnetization. *Phys. Rev. B* **105**, 064423 (2022).
55. Mahan, G. D. *Many-particle physics* (Springer Science & Business Media, 2013)
56. Tse, W.-K. & MacDonald, A. H. Giant magneto-optical kerr effect and universal faraday effect in thin-film topological insulators. *Phys. Rev. Lett.* **105**, 057401 (2010).
57. Lee, W.-R. & Tse, W.-K. Dynamical quantum anomalous hall effect in strong optical fields. *Phys. Rev. B* **95**, 201411 (2017).
58. Persky, E., Sochnikov, I. & Kalisky, B. Studying quantum materials with scanning squid microscopy. *Ann. Rev. Condens. Matter Phys.* **13**, null (2022).
59. Hong, S. et al. Nanoscale magnetometry with nv centers in diamond. *MRS Bull.* **38**, 155–161 (2013).
60. Glenn, D. R. et al. High-resolution magnetic resonance spectroscopy using a solid-state spin sensor. *Nature* **555**, 351–354 (2018).
61. Thiel, L. et al. Probing magnetism in 2d materials at the nanoscale with single-spin microscopy. *Science* **364**, 973–976 (2019).
62. Sun, Q.-C. et al. Magnetic domains and domain wall pinning in atomically thin crbr3 revealed by nanoscale imaging. *Nat. Commun.* **12**, 1–7 (2021).
63. Prem, A., Moroz, S., Gurarie, V. & Radzihovsky, L. Multiply quantized vortices in fermionic superfluids: angular momentum, unpaired fermions, and spectral asymmetry. *Phys. Rev. Lett.* **119**, 067003 (2017).
64. Zeng, J., Hou, T., Qiao, Z. & Tse, W.-K. Finite-size effects in the dynamic conductivity and faraday effect of quantum anomalous hall insulators. *Phys. Rev. B* **100**, 205408 (2019).
65. Seetharam, K. I., Bardyn, C.-E., Lindner, N. H., Rudner, M. S. & Refael, G. Controlled population of floquet-bloch states via coupling to bose and fermi baths. *Phys. Rev. X* **5**, 041050 (2015).
66. Matsuda, T. et al. Ultrafast dynamics of intrinsic anomalous hall effect in the topological antiferromagnet mn_3Sn. *Phys. Rev. Lett.* **130**, 126302 (2023).
67. Kirilyuk, A., Kimel, A. V. & Rasing, T. Ultrafast optical manipulation of magnetic order. *Rev. Mod. Phys.* **82**, 2731–2784 (2010).
68. Schüler, M. et al. How circular dichroism in time- and angle-resolved photoemission can be used to spectroscopically detect transient topological states in graphene. *Phys. Rev. X* **10**, 041013 (2020).
69. Schüler, M. et al. Local berry curvature signatures in dichroic angle-resolved photoelectron spectroscopy from two-dimensional materials. *Science advances* **6**, eaay2730 (2020).
70. Park, S. R. et al. Chiral orbital-angular momentum in the surface states of bi_2se_3. *Phys. Rev. Lett.* **108**, 046805 (2012).
71. Fukuyama, H. Theory of orbital magnetism of bloch electrons: Coulomb interactions. *Progr. Theor. Phys.* **45**, 704–729 (1971).
72. Gutiérrez-Rubio, A., Stauber, T., Gómez-Santos, G., Asgari, R. & Guinea, F. Orbital magnetic susceptibility of graphene and mos_2. *Phys. Rev. B* **93**, 085133 (2016).
73. Dehghani, H. & Mitra, A. Dynamical generation of superconducting order of different symmetries in hexagonal lattices. *Phys. Rev. B* **96**, 195110 (2017).
74. Claassen, M., Kennes, D. M., Zingl, M., Sentef, M. A. & Rubio, A. Universal optical control of chiral superconductors and majorana modes. *Nat. Phys.* **15**, 766–770 (2019).
75. Dehghani, H., Hafezi, M. & Ghaemi, P. Light-induced topological superconductivity via floquet interaction engineering. *Phys. Rev. Res.* **3**, 023039 (2021).
76. Kennes, D. M., Claassen, M., Sentef, M. A. & Karrasch, C. Light-induced *d*-wave superconductivity through floquet-engineered fermi surfaces in cuprates. *Phys. Rev. B* **100**, 075115 (2019).
77. Dehghani, H., Raines, Z. M., Galitski, V. M. & Hafezi, M. Optical enhancement of superconductivity via targeted destruction of charge density waves. *Phys. Rev. B* **101**, 224506 (2020).
78. Kitamura, S. & Aoki, H. Floquet topological superconductivity induced by chiral many-body interaction. *Commun. Phys.* **5**, 174 (2022).
79. Esin, I., Rudner, M. S., Refael, G. & Lindner, N. H. Quantized transport and steady states of floquet topological insulators. *Phys. Rev. B* **97**, 245401 (2018).

Acknowledgements

We thank Julia Sell and Bin Cao for helpful discussions. This work is supported by ARL W911NF1920181, AFOSR MURI FA9550-19-1-0399, AFOSR 95502010223, NSF DMR-2019444, ARO W911NF2010232, Minta Martin and Simons Foundations. M.H. thanks ETH Zurich for their hospitality during the conclusion of this work.

Author contributions

M.H. conceived the research. I.A. performed the calculations, and M.H. and H.D. supervised the study. M.H., H.D., and I.A. analyzed the data. I.A. wrote the first draft. M.H., I.A., and H.D. discussed the results and physical interpretation and wrote the final version of the manuscript.

Competing interests

The authors declare no competing interests.

Additional information

Supplementary information The online version contains supplementary material available at https://doi.org/10.1038/s42005-023-01267-0.

Correspondence and requests for materials should be addressed to Iman Ahmadabadi.

Peer review information *Communications Physics* thanks the anonymous reviewers for their contribution to the peer review of this work.

Reprints and permission information is available at http://www.nature.com/reprints

Publisher's note Springer Nature remains neutral with regard to jurisdictional claims in published maps and institutional affiliations.